

# Equivariant Filter for Tightly Coupled LiDAR-Inertial Odometry\*

Anbo Tao<sup>1</sup>, Yarong Luo<sup>2</sup>, Chunxi Xia<sup>1</sup>, Chi Guo<sup>2</sup>, and Xingxing Li<sup>1</sup>

**Abstract**—Pose estimation is a crucial problem in simultaneous localization and mapping (SLAM). However, developing a robust and consistent state estimator remains a significant challenge, as the traditional extended Kalman filter (EKF) struggles to handle the model nonlinearity, especially for inertial measurement unit (IMU) and light detection and ranging (LiDAR). To provide a consistent and efficient solution of pose estimation, we propose Eq-LIO, a robust state estimator for tightly coupled LIO systems based on an equivariant filter (EqF). Compared with the invariant Kalman filter based on the  $SE_2(3)$  group structure, the EqF uses the symmetry of the semi-direct product group to couple the system state including IMU bias, navigation state and LiDAR extrinsic calibration state, thereby suppressing linearization error and improving the behavior of the estimator in the event of unexpected state changes. The proposed Eq-LIO owns natural consistency and higher robustness, which is theoretically proven with mathematical derivation and experimentally verified through a series of tests on both public and private datasets.

**Index Terms**—LiDAR-inertial odometry, Equivariant filter.

## I. INTRODUCTION

In recent years, light detection and ranging (LiDAR) sensors have gained widespread use in simultaneous localization and mapping (SLAM) due to their ability to capture precise depth information. However, LiDAR is vulnerable to distortion caused by rapid movements. In contrast, inertial measurement units (IMUs) can provide motion data at high sampling rates regardless of external environmental conditions. IMU and LiDAR exhibit complementary characteristics, integrating these sensors can significantly enhance the continuity and accuracy of the output [1]–[3].

As a result, LiDAR-inertial odometry (LIO) has been widely used in industry. Among various approaches, filter-based methods are well-suited for low-cost platforms with limited computing resources, as they can efficiently handle large volumes of real-time measurements while maintaining lower computational demands. Among filter-based methods, the extended Kalman filter (EKF) achieves high efficiency, albeit with some loss of accuracy. This trade-off makes it a classic data fusion method, as seen in applications like [4] and others. However, researchers have identified that EKF may yield inconsistent estimates, where the computed

covariance deviates from the true covariance [5]. To alleviate the inconsistency problem, Barrau and Bonnabel proposed the invariant extended Kalman filter (IEKF) [6]. IEKF ensures the consistency of the bias-free IMU system by analyzing the system’s group affine properties. Later, Shi et al. [7] applied the IEKF for fusing IMU and LiDAR measurements to reduce estimation error, but the IMU bias will destroy the symmetry of the system. Mahony et al. proposed a modern method known as equivariant filtering (EqF) [8], [9], which naturally enhances consistency and robustness with lower computational overhead by incorporating different system symmetries and fixed linearization points. In light of these advantages, our work fully leverages EqF.

In this article, we introduce Eq-LIO, a fast and reliable tightly coupled LIO framework based on the EqF state estimator. Our approach leverages the semi-direct product group to incorporate symmetries, including bias and extrinsic parameters, into the LIO framework. Additionally, we optimize the gravity constraint on the manifold  $S^2$ . The error dynamics of the EqF ensures that it always performs linearization operations at a fixed origin, which is the key to improving system consistency and reducing linearization errors. Finally, we validate the performance of Eq-LIO in both standard and challenging scenarios. The main contributions of our work are as follows:

- 1) We introduce Eq-LIO, a tightly coupled LIO system based on the EqF state estimator, with LiDAR and IMU self-calibration capabilities and gravity constraints on  $S^2$ . To the best of our knowledge, this is the first LIO system to utilize an equivariant filter.
- 2) We perform extensive benchmark testing across diverse datasets, demonstrating that the proposed framework delivers superior accuracy, robustness, and consistency without increasing computational demands. To support community development, our source code is available online: <https://github.com/Eliaul/Eq-LIO>.

## II. RELATED WORKS

In this section, we focus on the most related works on LIO and Kalman filtering.

### A. LiDAR-Inertial Odometry

LIO methods can be broadly categorized into two approaches: loosely coupled methods and tightly coupled methods. Loosely coupled methods typically process measurements from the IMU and LiDAR independently before fusing the results. For instance, the LOAM algorithm proposed in [10]

<sup>1</sup>Anbo Tao, Chunxi Xia and Xingxing Li are with the School of Geodesy and Geomatics, Wuhan University, China. {tao\_ab,xiachunxi}@whu.edu.cn, xxli@sgg.whu.edu.cn

<sup>2</sup>Yarong Luo and Chi Guo are with the GNSS Research Center, Wuhan University, China. {yarongluo,guochi}@whu.edu.cn

\*This work is supported in part by the China Postdoctoral Science Foundation under Grant Number(2023TQ0248) and in part by the National Key Research and Development Program of China under Grant 2021YFB2501102 and 2023YFB3907100 (Corresponding author: Yarong Luo).

utilized the pose estimated from IMU data as an initial guess for LiDAR scan registration. In [11], an adaptive EKF was employed to fuse IMU measurements with poses estimated by LiDAR SLAM, enhancing the accuracy of pose estimation. The direct LiDAR odometry method introduced in [12] enabled real-time, high-speed, and high-precision processing of dense point clouds. While loosely coupled methods offer high computational efficiency, their limited ability to effectively fuse sensor data may lead to unreliable results in the later stages of the fusion process.

The tightly coupled methods directly fuse LiDAR point cloud data with IMU measurements to obtain an optimal state estimation, which can be divided into two primary categories: optimization-based methods and filter-based methods. For optimization-based methods, Ye et al. [1] introduced the LIOM framework, which applied sliding window optimization to LIO. Similarly, LIO-SAM [2] employed smoothing and mapping techniques to achieve sensor fusion and global optimization. In filter-based methods, LINS [3] utilized a robo-centric iterative Kalman filter for tightly coupled pose optimization. FAST-LIO [13] utilized a world-centric iterative Kalman filtering for state estimation, incorporating a novel Kalman gain formula to enhance computational efficiency. FAST-LIO2 [14] further improved system efficiency and robustness by using direct point cloud registration and an ikd-tree structure.

### B. Kalman Filtering for Navigation Applications

Since the introduction of the classic extended Kalman filter (EKF), it has become a widely used tool in filter-based SLAM algorithms. However, the traditional EKF-based LIO algorithm is susceptible to overconfidence issues due to spurious information gain in unobservable directions. To address the inconsistency issues inherent in EKF, Barrau and Bonnabel proposed the invariant extended Kalman filter (IEKF) [6], demonstrating that a consistent filtering algorithm can be developed on group affine systems. This method assumes that the IMU is bias-free, which could not be ignored in practical applications. Despite this limitation, many researchers [15], [16] continue to use this imperfect IEKF framework in the design of SLAM algorithms. They defined the IMU bias on  $\mathbb{R}^3$ , which destroys the group affine property of the system. Recently, SuIn-LIO [17] was proposed, combining an IEKF with an efficient surfel-based map to achieve high-precision LIO. Shi et al. [7] applied the IEKF to the robo-centric and world-centric based LIO and demonstrated that the world-centric method achieves a higher level of accuracy.

Unlike IEKF, which parameterizes the state using Lie groups, Mahony et al. developed an equivariant filtering (EqF) framework [8], [18] that generalizes the state space from Lie groups to homogeneous manifolds. Additionally, EqF does not require constant changes to the linearization point, which naturally ensures system consistency. Subsequently, Fornasier et al. applied EqF to an inertial navigation system [19], which accounts for bias, and demonstrated that various filters, including the EKF, can be incorporated within the EqF framework

[20]. Recently, Fornasier et al. [21] introduced an equivariant filter design for vision-assisted INS systems. This new design has been demonstrated to outperform state-of-the-art methods in both robustness and transient behavior.

## III. MATHEMATICAL PRELIMINARIES AND NOTATION

### A. Smooth Manifolds and Lie Theory

Let  $\mathcal{M}$  be a smooth manifold, we use  $T_\xi\mathcal{M}$  to denote the tangent space of  $\mathcal{M}$  at point  $\xi \in \mathcal{M}$  and  $T\mathcal{M}$  to denote the tangent bundle. The notion  $\mathfrak{X}(\mathcal{M})$  denotes the set of smooth vector field on  $\mathcal{M}$ , where each element of  $\mathfrak{X}(\mathcal{M})$  assigns a tangent vector in  $T_\xi\mathcal{M}$  to each point  $\xi \in \mathcal{M}$ . A Lie group  $G$  is a smooth manifold with a group structure, and group multiplication and inversion operations are smooth as mappings between manifolds. For any elements  $X, Y \in G$ , the group multiplication is denoted by  $XY$ , the inverse of  $X$  is denoted by  $X^{-1}$ , the identity is denoted by  $I$ . The tangent space of  $G$  at  $I$  is called the Lie algebra of  $G$ , denoted by  $\mathfrak{g}$ , that is,  $\mathfrak{g} = T_I G$ . The Lie algebra  $\mathfrak{g}$  is a vector space with dimension equal to  $n = \dim G$ . So we have an isomorphism from  $\mathfrak{g}$  to  $\mathbb{R}^n$ , which we denote  $(\cdot)^\vee : \mathfrak{g} \rightarrow \mathbb{R}^n$ , and the inverse of  $(\cdot)^\vee$  is  $(\cdot)^\wedge : \mathbb{R}^n \rightarrow \mathfrak{g}$ . In this work, we focus only on the Lie group of matrices, i.e.,  $G$  is a subgroup of the general linear group  $GL_n(\mathbb{R})$ .

Fixing a point  $X \in G$ , there are two important mappings  $L_X : G \rightarrow G$  and  $R_X : G \rightarrow G$ , which are called left translation and right translation respectively:

$$L_X(Y) = XY, \quad R_X(Y) = YX.$$

Given an element  $X \in G$ , consider the conjugate action  $Y \mapsto XYX^{-1}$  on the Lie group. The differential of this action at the identity  $I$  is

$$\text{Ad}_X : \mathfrak{g} \rightarrow \mathfrak{g}, \quad \text{Ad}_X(\mathbf{u}) = (dL_X) \circ (dR_{X^{-1}})(\mathbf{u}),$$

for every  $\mathbf{u} \in \mathfrak{g}$ . This map  $\text{Ad}_X$  is called a (big) Adjoint map. Since we have an isomorphism  $(\cdot)^\vee : \mathfrak{g} \rightarrow \mathbb{R}^n$ ,  $\text{Ad}_X^\vee := (\cdot)^\vee \circ \text{Ad}_X \circ (\cdot)^\wedge$ , as a linear map  $\mathbb{R}^n \rightarrow \mathbb{R}^n$ , can be viewed as a matrix.

For any  $\mathbf{u} \in \mathfrak{g}$ , the (little) adjoint map is defined by

$$\text{ad}_\mathbf{u} : \mathfrak{g} \rightarrow \mathfrak{g}, \quad \text{ad}_\mathbf{u}(v) = [u, v],$$

where  $[u, v]$  is the Lie bracket.

### B. Group Action, Useful Maps and Notation Explanation

Assuming  $G$  is a Lie group and  $\mathcal{M}$  is a smooth manifold, we consider the Lie group action  $\phi : G \times \mathcal{M} \rightarrow \mathcal{M}$ . Fixing an element  $X \in G$ , we write  $\phi_X : \mathcal{M} \rightarrow \mathcal{M}$  to represent

$$\phi_X(\xi) := \phi(X, \xi).$$

Fix an element  $\xi \in \mathcal{M}$ , we write  $\phi^{(\xi)} : G \rightarrow \mathcal{M}$  to represent

$$\phi^{(\xi)}(X) := \phi(X, \xi).$$

For all  $\mathbf{X} = (\mathbf{C}, \mathbf{a}, \mathbf{b}) \in \text{SE}_2(3) = \text{SO}(3) \ltimes (\mathbb{R}^3 \oplus \mathbb{R}^3)$ , define  $\Gamma$  to extract the rotation part of  $\mathbf{X}$ :

$$\Gamma : \text{SE}_2(3) \rightarrow \text{SO}(3), \quad \Gamma(\mathbf{X}) = \mathbf{C}.$$

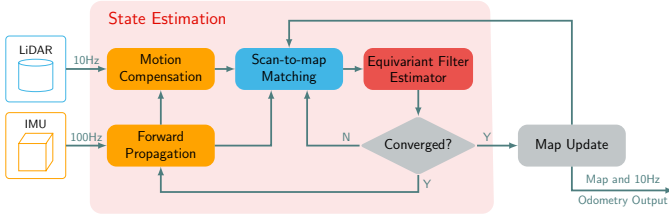


Fig. 1. Overview of Eq-LIO. The equivariant filtering state estimator is employed in the odometry module, with the measurement model constructed through scan-to-map matching. The red box in the figure highlights the main content of this paper. For detailed information, please refer to Section IV and V.

In this article, the use of bold and non-bold letters for the same character represents two different meanings. Bold letters are generally used to denote matrices, while non-bold letters are typically used to represent elements in groups or manifolds.

#### IV. SYSTEM OVERVIEW

The pipeline of the proposed Eq-LIO is illustrated in Fig. 1. The raw point cloud is first de-skewed using IMU predicted pose [14]. Next, a world-centric equivariant filter state estimator is constructed for the odometry module, utilizing the scan-to-map matching method to establish correspondence between the LiDAR scan and the global map. Finally, the output from the state estimator is used to update the global map.

##### A. System Definition

The IMU coordinate system at the origin is used as the reference coordinate system, which we call the world coordinate system and is represented by  $w$ . We use  $b$  to represent the body coordinate system. The system model of LIO is as follows.

$$\begin{aligned}
 \dot{C}_b^w &= C_b^w (\boldsymbol{\omega} - \mathbf{b}_g)^\wedge, \\
 \dot{\mathbf{v}}_{wb}^w &= C_b^w (\mathbf{a} - \mathbf{b}_a) + \mathbf{g}^w, \\
 \dot{\mathbf{r}}_{wb}^w &= \mathbf{v}_{wb}^w, \\
 \dot{\mathbf{b}}_g &= \mathbf{0}_{3 \times 1}, \quad \dot{\mathbf{b}}_a = \mathbf{0}_{3 \times 1}, \\
 \dot{C}^b &= \mathbf{O}_{3 \times 3}, \quad \dot{\mathbf{l}}^b = \mathbf{0}_{3 \times 1},
 \end{aligned} \tag{1}$$

where  $C_b^w$ ,  $\mathbf{v}_{wb}^w$ ,  $\mathbf{r}_{wb}^w$  represents the attitude, velocity and position of the IMU,  $\mathbf{b}_g$  and  $\mathbf{b}_a$  represent the gyroscope bias and accelerometer bias, respectively, and  $C^b$  and  $\mathbf{l}^b$  represent the attitude and position of the LiDAR relative to the IMU,  $\mathbf{g}^w$  represents the gravity vector,  $\boldsymbol{\omega}$  and  $\mathbf{a}$  represent the angular velocity and specific force measured by the IMU.

We introduce a virtual ‘‘velocity bias’’  $\mathbf{b}_\mu$  and virtual inputs  $\boldsymbol{\mu}$ ,  $\boldsymbol{\tau}_c$ ,  $\boldsymbol{\tau}_g$ ,  $\boldsymbol{\tau}_a$ ,  $\boldsymbol{\tau}_\mu$ ,  $\boldsymbol{\tau}_l$  to exploit the geometric properties of the system, the equation (1) expands to [19]:

$$\begin{aligned}
 \dot{C}_b^w &= C_b^w (\boldsymbol{\omega} - \mathbf{b}_g)^\wedge, & \dot{\mathbf{b}}_g &= \boldsymbol{\tau}_g, \\
 \dot{\mathbf{v}}_{wb}^w &= C_b^w (\mathbf{a} - \mathbf{b}_a) + \mathbf{g}^w, & \dot{\mathbf{b}}_a &= \boldsymbol{\tau}_a, \\
 \dot{\mathbf{r}}_{wb}^w &= C_b^w (\boldsymbol{\mu} - \mathbf{b}_\mu) + \mathbf{v}_{wb}^w, & \dot{\mathbf{b}}_\mu &= \boldsymbol{\tau}_\mu, \\
 \dot{C}^b &= C^b \boldsymbol{\tau}_c^\wedge, & \dot{\mathbf{l}}^b &= \boldsymbol{\tau}_l.
 \end{aligned} \tag{2}$$

The system state is modeled as  $\xi = (\mathbf{T}, \mathbf{b}^\wedge, \mathbf{K}) \in \mathcal{M}$ , with navigation state  $\mathbf{T} = (C_b^w, \mathbf{v}_{wb}^w, \mathbf{r}_{wb}^w) \in \text{SE}_2(3)$ , bias  $\mathbf{b} = (\mathbf{b}_g, \mathbf{b}_a, \mathbf{b}_\mu) \in \mathbb{R}^9$  and extrinsic parameters  $\mathbf{K} = (C^b, \mathbf{l}^b) \in \text{SE}(3)$  of LiDAR and IMU. Let  $\mathbf{u} = (\boldsymbol{\omega}^\wedge, \mathbf{g}^\wedge, \boldsymbol{\tau}^\wedge, \boldsymbol{\tau}_k^\wedge) \in (\mathfrak{se}_2(3))^3 \times \mathfrak{se}(3)$  be the system inputs, where  $\mathbf{g}^\wedge = (\mathbf{0}^\wedge, \mathbf{g}^w, \mathbf{0}) \in \mathfrak{se}_2(3)$ ,  $\boldsymbol{\tau}^\wedge = (\boldsymbol{\tau}_g^\wedge, \boldsymbol{\tau}_a, \boldsymbol{\tau}_u) \in \mathfrak{se}_2(3)$ ,  $\boldsymbol{\tau}_k^\wedge = (\boldsymbol{\tau}_c^\wedge, \boldsymbol{\tau}_l) \in \mathfrak{se}(3)$  and  $\boldsymbol{w} = (\boldsymbol{\omega}, \mathbf{a}, \boldsymbol{\mu})$  be the IMU measurements. In general, the system state evolves on the manifold  $\mathcal{M} = \text{SE}_2(3) \times \mathfrak{se}_2(3) \times \text{SE}(3)$ , and the system inputs are in the input space  $L = (\mathfrak{se}_2(3))^3 \times \mathfrak{se}(3)$ . In this notation, the system model (2) can be rewritten as

$$\begin{aligned}
 \dot{\mathbf{T}} &= f_1^0(\mathbf{T})\mathbf{T} + \mathbf{T}(\boldsymbol{\omega}^\wedge - \mathbf{b}^\wedge) + \mathbf{g}^\wedge \mathbf{T}, \\
 \dot{\mathbf{b}} &= \boldsymbol{\tau}, \\
 \dot{\mathbf{K}} &= \mathbf{K} \boldsymbol{\tau}_k^\wedge,
 \end{aligned} \tag{3}$$

where  $f_1^0 : \text{SE}_2(3) \rightarrow T\text{SE}_2(3)$  defined by  $\mathbf{X} = (C, \mathbf{v}, \mathbf{r}) \mapsto (\mathbf{O}, \mathbf{0}, \mathbf{v}) \in T_{\mathbf{X}}\text{SE}_2(3)$  is a vector field on  $\text{SE}_2(3)$ . We can write (3) in a more compact form:

$$\begin{aligned}
 \dot{\xi} &= f^0(\xi) + f_u(\xi) \\
 &= f^0(\xi) + (\mathbf{T}(\boldsymbol{w} - \mathbf{b})^\wedge + \mathbf{g}^\wedge \mathbf{T}, \boldsymbol{\tau}^\wedge, \mathbf{K} \boldsymbol{\tau}_k^\wedge),
 \end{aligned} \tag{4}$$

where  $f^0 : \mathcal{M} \rightarrow T\mathcal{M}$  defined by  $\xi \mapsto (f_1^0(\mathbf{T}), \mathbf{O}, \mathbf{O}) \in T_\xi \mathcal{M}$  is a vector field on  $\mathcal{M}$ .

##### B. Equivariant Symmetry of the System

The symmetry of the system arises from the key semidirect product group  $G = (\text{SE}_2(3) \ltimes \mathfrak{se}_2(3)) \times \text{SE}(3)$ . Let  $X = (A, a^\wedge, B) \in G$ ,  $\gamma = (\gamma_1^\wedge, \gamma_2^\wedge, \gamma_3^\wedge, \gamma_4^\wedge) \in L$ .

*Proposition 4.1:* Define  $\phi : G \times \mathcal{M} \rightarrow \mathcal{M}$  as

$$\phi(X, \xi) = (\mathbf{T}A, \text{Ad}_{A^{-1}}(\mathbf{b}^\wedge - a^\wedge), \Gamma(A)^{-1} \mathbf{K}B), \tag{5}$$

where  $\text{Ad}_{A^{-1}} : \mathfrak{se}_2(3) \rightarrow \mathfrak{se}_2(3)$  represents the isomorphism induced by conjugation  $Y \mapsto A^{-1}YA$  on  $\text{SE}_2(3)$ . Then  $\phi$  is a transitive and free right group action of  $G$  on  $\mathcal{M}$  [22].

*Proposition 4.2:* Define  $\psi : G \times L \rightarrow L$  as

$$\begin{aligned}
 \psi(X, \gamma) &= (\text{Ad}_{A^{-1}}(\gamma_1^\wedge - a^\wedge) + f_1^0(A^{-1}), \\
 &\quad \gamma_2^\wedge, \text{Ad}_{A^{-1}} \gamma_3^\wedge, \text{Ad}_{B^{-1}} \gamma_4^\wedge),
 \end{aligned} \tag{6}$$

then  $\psi$  is a right group action of  $G$  on  $L$ .

*Theorem 4.3:* System (4) is equivariant with group action in Proposition 4.1 and Proposition 4.2, that is,

$$\begin{aligned}
 f^0(\xi) + f_{\psi_X(\gamma)}(\xi) \\
 = d\phi_X(f^0(\phi_{X^{-1}}(\xi)) + f_\gamma(\phi_{X^{-1}}(\xi)))
 \end{aligned} \tag{7}$$

for every  $X \in G, \xi \in \mathcal{M}$  and  $\gamma \in L$ .

##### C. Lifted System

Equivariant filtering requires a lift  $\Lambda : \mathcal{M} \times L \rightarrow \mathfrak{g}$  to transfer the system differential equations to the Lie group  $G$ . The lift  $\Lambda$  requires

$$d\phi^{(\xi)} \circ \Lambda(\xi, \gamma) = f_\gamma(\xi),$$

where  $\xi \in \mathcal{M}$  and  $\gamma \in L$ . If the group action  $\phi$  is transitive, then such a lift always exists.

*Theorem 4.4:* Define  $\Lambda_1 : \mathcal{M} \times L \rightarrow \mathfrak{se}_2(3)$  as

$$\Lambda_1(\xi, \gamma) = \gamma_1^\wedge - \mathbf{b}^\wedge + \text{Ad}_{\mathbf{T}^{-1}} \gamma_2^\wedge + \mathbf{T}^{-1} f_1^0(\mathbf{T}),$$

$\Lambda_2 : \mathcal{M} \times L \rightarrow \mathfrak{se}_2(3)$  as

$$\Lambda_2(\xi, \gamma) = \text{ad}_{\mathbf{b}^\wedge}(\Lambda_1(\xi, \gamma)) - \gamma_3^\wedge,$$

$\Lambda_3 : \mathcal{M} \times L \rightarrow \mathfrak{se}(3)$  as

$$\Lambda_3(\xi, \gamma) = \text{Ad}_{\mathbf{K}^{-1}}[\Gamma(\Lambda_1(\xi, \gamma))] + \gamma_4^\wedge,$$

then  $\Lambda : \mathcal{M} \times L \rightarrow \mathfrak{g} = \mathfrak{se}_2(3) \oplus \mathfrak{se}_2(3) \oplus \mathfrak{se}(3)$

$$\Lambda(\xi, \gamma) = (\Lambda_1(\xi, \gamma), \Lambda_2(\xi, \gamma), \Lambda_3(\xi, \gamma)) \quad (8)$$

is an equivariant lift [19].

Let  $X \in G$  be the state on the Lie group, and  $\xi^0 \in \mathcal{M}$  be the original state. If the group action  $\phi$  is free, then the lift  $\Lambda$  leads to a system on Lie group  $G$ :

$$\dot{X} = dL_X \circ \Lambda(\phi(\xi^0)(X), \gamma). \quad (9)$$

This transformation moves the estimation problem from the manifold to the Lie group, allowing the error to be defined via multiplication on the Lie group.

If the estimated error covariance reflects the true distribution of the errors, then the estimator is said to be consistent. The consistency of the system can be proven using the group action  $\phi$  in equation (5) and the lift  $\Lambda$  in equation (8) [23], [24].

## V. EQUIVARIANT FILTER

### A. Error Dynamics

For a state  $\xi \in \mathcal{M}$ , define  $e = \phi_{\hat{X}^{-1}}(\xi) \in \mathcal{M}$  to represent the error on the manifold  $\mathcal{M}$  [25]. Choose a local coordinate map  $\varphi : U \rightarrow \mathbb{R}^9 \oplus \mathbb{R}^9 \oplus \mathbb{R}^6$  at the origin  $\xi^0$ ,  $\varphi$  can be taken as

$$\varphi(e) = (\log^\vee e_1, e_2^\vee, \log^\vee e_3).$$

Let  $\varepsilon = \varphi(e) \in \mathbb{R}^{24}$ . The linear error  $\varepsilon$  satisfies the differential equation

$$\dot{\varepsilon} \approx \mathbf{F}\varepsilon,$$

$$\mathbf{F} = (d\varphi)_{\xi^0} \circ (d\phi^{\xi^0})_I \circ (d\Lambda_{\mathbf{u}})_{\xi^0} \circ (d\varphi^{-1})_{\mathbf{0}}.$$

The closed-form of the matrix  $\mathbf{F}$  is

$$\mathbf{F} = \begin{bmatrix} \mathbf{F}_T & -\mathbf{I}_{9 \times 9} & \mathbf{O}_{9 \times 6} \\ \mathbf{O}_{9 \times 9} & \mathbf{F}_b & \mathbf{O}_{9 \times 6} \\ \mathbf{O}_{6 \times 9} & \mathbf{O}_{6 \times 9} & \mathbf{F}_K \end{bmatrix} \in \mathbb{R}^{24 \times 24}, \quad (10)$$

where

$$\mathbf{F}_T = \begin{bmatrix} \mathbf{g}^{w^\wedge} & \\ & \mathbf{I}_{3 \times 3} \end{bmatrix} \in \mathbb{R}^{9 \times 9},$$

$$\mathbf{F}_b = \begin{bmatrix} \mathbf{W} & & & \\ \mathbf{Y} & \mathbf{W} & & \\ \mathbf{Z} & & \mathbf{W} & \end{bmatrix} \in \mathbb{R}^{9 \times 9}, \mathbf{F}_K = \begin{bmatrix} \mathbf{W} & \\ \mathbf{Z} & \mathbf{W} \end{bmatrix} \in \mathbb{R}^{6 \times 6},$$

$$\mathbf{Y} = (\hat{\mathbf{C}}_b^w(\mathbf{a} - \hat{\mathbf{b}}_a) + (\hat{\mathbf{v}}_{wb}^w)^\wedge \hat{\mathbf{C}}_b^w(\boldsymbol{\omega} - \hat{\mathbf{b}}_g) + \mathbf{g}^w)^\wedge,$$

$$\mathbf{Z} = (\hat{\mathbf{C}}_b^w(\boldsymbol{\mu} - \hat{\mathbf{b}}_\mu) + (\hat{\mathbf{r}}_{wb}^w)^\wedge \hat{\mathbf{C}}_b^w(\boldsymbol{\omega} - \hat{\mathbf{b}}_g) + \hat{\mathbf{v}}_{wb}^w)^\wedge,$$

$$\mathbf{W} = (\hat{\mathbf{C}}_b^w(\boldsymbol{\omega} - \hat{\mathbf{b}}_g))^\wedge.$$

The letters with hat in them represent the estimated value of that state and  $\mathbf{I}$  represents the identity matrix.

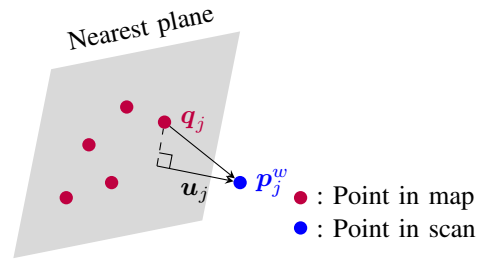


Fig. 2. The measurement model.

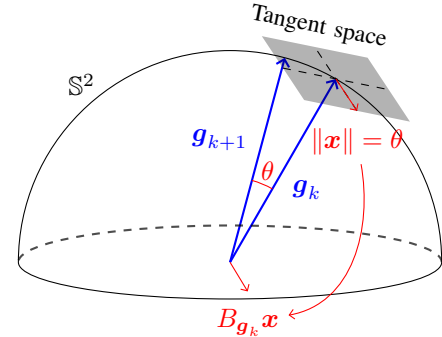


Fig. 3. Illustration of the error state on  $\mathbb{S}^2$ . The neighborhood at  $\mathbf{g}_k \in \mathbb{S}^2$  is homeomorphic to  $\mathbb{R}^2$ .  $\mathbf{x}$  is a minimal parameterization of the error between  $\mathbf{g}_{k+1}$  with  $\mathbf{g}_k$ .

### B. Measurement Model

At a certain moment, the LiDAR acquires  $m$  sampling points  $\{\mathbf{p}_j\}_{j=1}^m$ . For each point  $\mathbf{p}_j$ , We denote point  $\mathbf{p}_j$  transformed to the world coordinate system as  $\mathbf{p}_j^w := \mathbf{C}_b^w(\mathbf{C}^b \mathbf{p}_j + \mathbf{l}^b) + \mathbf{r}_{wb}^w$ . Search for the five points closest to  $\mathbf{p}_j^w$  and fit a plane, then  $\mathbf{p}_j^w$  should be in this plane (Fig. 2). Therefore, the system output  $h_j : \mathcal{M} \rightarrow \mathbb{R}$  can be configured as [14]

$$h_j(\xi) = \mathbf{n}_j^\top (\mathbf{p}_j^w - \mathbf{q}_j),$$

where  $\mathbf{n}_j$  is the normal vector of the plane and  $\mathbf{q}_j$  is an arbitrary point in the plane.

According to [8], the linearized measurement equation is

$$\mathbf{z}_j = \mathbf{H}_j \varepsilon, \mathbf{H}_j = (dh_j)_{\xi} \circ (d\phi_{\hat{X}})_{\xi^0} \circ (d\varphi^{-1})_{\mathbf{0}}.$$

The closed-form of the matrix  $\mathbf{H}_j$  is

$$\mathbf{H}_j = [\mathbf{H}_{j,T} \quad \mathbf{O}_{1 \times 9} \quad \mathbf{H}_{j,K}] \in \mathbb{R}^{1 \times 24}, \quad (11)$$

where

$$\mathbf{H}_{j,T} = [-\mathbf{n}_j^\top \mathbf{p}_j^{w^\wedge} \quad \mathbf{O}_{1 \times 3} \quad \mathbf{n}_j^\top] \in \mathbb{R}^{1 \times 9},$$

$$\mathbf{H}_{j,K} = [-\mathbf{n}_j^\top \mathbf{p}_j^{w^\wedge} \quad \mathbf{n}_j^\top] \in \mathbb{R}^{1 \times 6}.$$

### C. Gravity Constraints on Manifolds $\mathbb{S}^2$

We consider gravity to be a vector with constant magnitude and direction on the sphere  $\mathbb{S}^2$ . Since  $\mathbb{S}^2$  is a two-dimensional manifold, we use a two-dimensional vector in the tangent space  $T_{\mathbf{g}} \mathbb{S}^2 \simeq \mathbb{R}^2$  as the error state for optimization, which uses the fewest degrees of freedom to estimate gravity.

TABLE I  
DISTANCE ERRORS ON THE LiLi-OM DATASET

Error(m)	FAST-LIO2	IEKF	EqF
<i>Schloss-1</i>	0.60	0.57	<b>0.53</b>
<i>Schloss-2</i>	11.50	8.75	<b>7.07</b>
<i>Campus-1</i>	0.97	0.78	<b>0.46</b>

Define the direction vector of gravity as  $\mathbf{g} = (x, y, z)^\top \in \mathbb{S}^2$  and  $\|\mathbf{g}\| = 1$ . Consider the linear map [26], [27]

$$B_{\mathbf{g}} : \mathbb{R}^2 \rightarrow \mathbb{R}^3 \quad B_{\mathbf{g}} = \begin{bmatrix} 1 - \frac{x^2}{1+z} & -\frac{xy}{1+z} \\ -\frac{xy}{1+z} & 1 - \frac{y^2}{1+z} \\ -x & -y \end{bmatrix}. \quad (12)$$

$B_{\mathbf{g}}$  is an isometry operator, that is,  $\|B_{\mathbf{g}}\mathbf{x}\| = \|\mathbf{x}\|$  for all  $\mathbf{x} \in \mathbb{R}^2$ . Through  $B_{\mathbf{g}}$ , we can convert the vector in the tangent space  $T_{\mathbf{g}}\mathbb{S}^2 \simeq \mathbb{R}^2$  into a rotation vector, thereby updating the gravity. The pseudoinverse of the matrix  $B_{\mathbf{g}}$  is  $B_{\mathbf{g}}^\top$ .

Denote the direction of gravity at time  $k$  by  $\mathbf{g}_k \in \mathbb{S}^2$  and the error state of the optimal estimate by  $\mathbf{x} \in \mathbb{R}^2$ . As shown in Fig. 3, we take

$$\mathbf{g}_{k+1} = \exp(B_{\mathbf{g}_k}\mathbf{x})\mathbf{g}_k \in \mathbb{S}^2.$$

Conversely, for the two gravity directions  $\mathbf{g}_k$  and  $\mathbf{g}_{k+1}$ , the error is defined as

$$\varepsilon_{\mathbf{g}} = \arccos(\mathbf{g}_k \cdot \mathbf{g}_{k+1})B_{\mathbf{g}_k}^\top(\mathbf{g}_k \times \mathbf{g}_{k+1}), \quad (13)$$

where  $\mathbf{g}_k \cdot \mathbf{g}_{k+1}$  represents the dot product of the vectors.

## VI. EXPERIMENTS

In this section, we conduct a series of experiments to evaluate the accuracy and robustness of Eq-LIO. In all experiments, we compare Eq-LIO with the IEKF-based LIO algorithm and the EKF-based FAST-LIO2 algorithm. Furthermore, for fairness, all algorithms use the same tuning parameters in the experiments.

### A. Public Datasets

1) *Public LiLi-OM Dataset*: Given LiLi-OM dataset [28] has no precise ground truth, we use the start-end distance as an indicator to roughly estimate accuracy of LIO. It is worth noting that the reference value is calculated by GNSS positioning results. The distance error for the LiLi-OM dataset is presented in Table I. The results show that the proposed Eq-LIO achieves the best accuracy on the three sequences, whereas the accuracy of FAST-LIO2 and IEKF on the *Schloss-2* dataset decreases significantly. In addition, Fig. 4 shows the time series of the three-axis gyroscope bias in the *Schloss-1* dataset. Interestingly, the proposed Eq-LIO exhibits the ability of the filter to converge quickly.

2) *Public R3LIVE Dataset*: In the R3LIVE [29] dataset, we use datasets with closed trajectories so that we can evaluate the end-to-end error. The end-to-end error results we obtained are shown in Table II. In most scenarios, Eq-LIO delivers superior results. However, in certain cases, such as the sequence

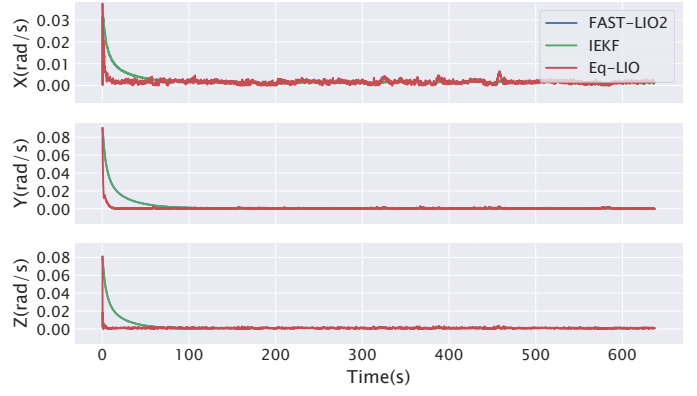


Fig. 4. The estimated three-axis gyroscope bias sequence in the *Schloss-1* dataset.

*hkust\_campus\_01*, the scan-to-map matching strategy used by FAST-LIO2 improves loop accuracy but also introduces the risk of matching errors, which will cause large jumps in the trajectory, as illustrated in Fig.5, while Eq-LIO does not have this problem. The speed curve is used here because it is easier to observe such jumps.

TABLE II  
END-TO-END ERRORS ON THE R3LIVE DATASET

Error(m)	FAST-LIO2	IEKF	EqF
<i>hku_campus_00</i>	0.17	0.07	<b>0.06</b>
<i>hkust_campus_00</i>	3.10	3.59	<b>2.26</b>
<i>hkust_campus_01</i>	<b>0.13</b>	1.51	0.19
<i>hkust_campus_02</i>	0.04	<b>0.03</b>	0.09
<i>degenerate_00</i>	8.25	6.23	<b>6.02</b>

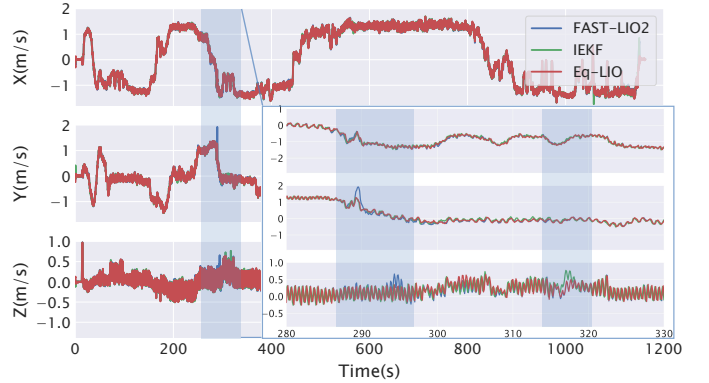


Fig. 5. Time series plot of the estimated velocities of the three axes in the *hkust\_campus\_01* dataset.

### B. Private Datasets

1) *Indoor Experiment*: Robustness is a crucial characteristic of filter-based LiDAR-inertial odometry, referring to the system's ability to withstand adverse external disturbances such as imperfect tuning parameters, degenerate motion scenes, or sustained intense movement. To induce significant changes in both rotation and velocity, the data collectors held the sensor in their hands and ran irregularly indoors, generating large and unpredictable movements. The data were collected

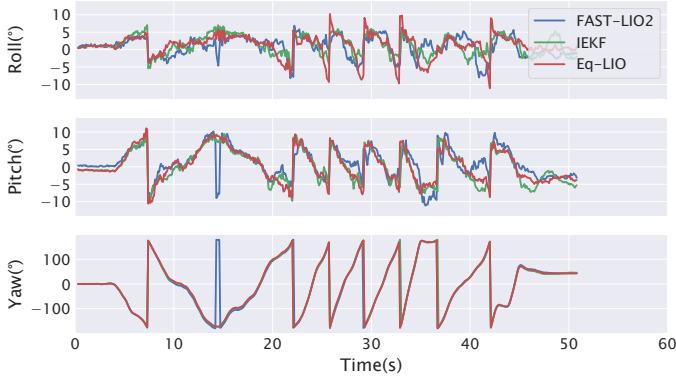


Fig. 6. Estimated attitude sequences in the indoor experiment.

using a Livox Avia LiDAR and its built-in MEMS IMU, with sampling frequencies of 100 Hz for LiDAR and 10 Hz for the IMU. Fig. 6 illustrates the attitude estimation during the experiment, revealing dramatic changes in a short period, making it ideal for examining the robustness of the proposed system. The results, depicted in Fig. 7, demonstrate that Eq-LIO produces the clearest mapping result and handles wall corners more effectively than IEKF. The mapping results of EKF-based FAST-LIO2 exhibit significant drift, while Eq-LIO shows less distortion on the walls, with the upper right corner of the map appearing clearer. This suggests that when handling highly nonlinear motion scenarios, the model based on Eq-LIO exhibits a superior linearization effect, making it more resilient to significant parameter errors and demonstrating enhanced robustness.

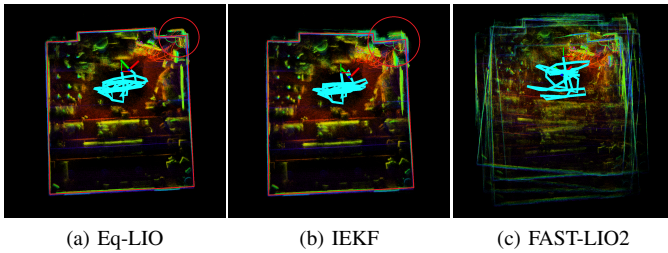


Fig. 7. Mapping results of LIO in the indoor high-speed environment based on three different filtering algorithms. The mapping results of FAST-LIO2 for this data set are not available. The red lines depict the wall of the EqF and IEKF mapping results, which can reflect the degree of deformation of the wall.

2) *Outdoor Experiment:* To verify the performance of Eq-LIO in actual urban complex scenes, we collected data from real urban highway scenes. The dataset was collected on roads in Wuhan and includes challenging scenarios such as long straight lines and large arc U-turns. The presence of many moving vehicles further complicates achieving robust navigation. The hardware platform for data collection is as follows: a GNSS receiver (Septentrio PolaRx5), GNSS antenna (Trimble Zephyr Model2), a MEMS IMU (ADIS-16470), a tactical IMU (StarNeto XW-GI7660), and a mechanical LiDAR (Velodyne

VLP-32) were rigidly fixed on an iron plate with roughly pre-calibrated extrinsic parameters. We used the MEMS IMU for testing and the tactical IMU with RTK/INS to generate reference ground truth.

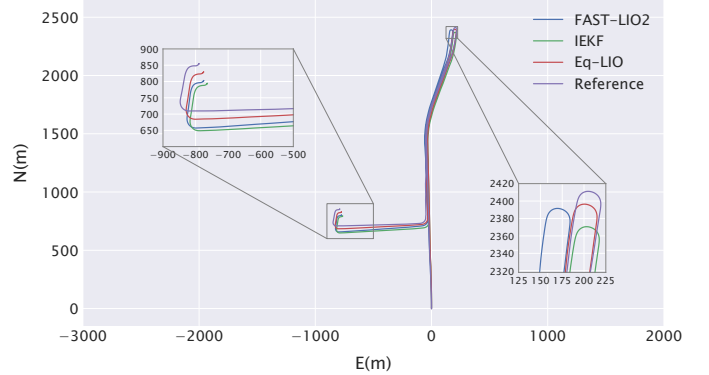


Fig. 8. Trajectories estimated by three filter-based LIO algorithms in the outdoor experiment.

TABLE III  
PLANAR DISTANCE ERRORS AT THE END OF THE TRAJECTORY IN THE OUTDOOR EXPERIMENT.

	E(m)	N(m)	Plane(m)
FAST-LIO2	14.309	51.725	53.668
IEKF	25.079	60.302	65.309
Eq-LIO	<b>13.899</b>	<b>25.124</b>	<b>28.713</b>

As shown in Fig. 8, all algorithms exhibit some errors due to the long trajectory and the presence of numerous moving objects. However, at both the U-turn and the end of the trajectory, the proposed Eq-LIO demonstrates superior performance, accurately estimating the scale of trajectory. Table III shows the planar distance errors of different algorithms at the final moment. The trajectory length is approximately 5132 meters, with Eq-LIO exhibiting the smallest drift in both the east and north directions. The vehicle primarily traveled along the north-south axis, resulting in more significant inconsistency in the northward direction. The results indicate that Eq-LIO produces smaller errors under erroneous observations compared to IEKF and EKF, demonstrating superior consistency in the northward direction.

## VII. CONCLUSION

This article presents Eq-LIO. To address the inconsistency and linearization point issues of traditional filtering algorithms, this work develops an equivariant filter for LIO systems, derives a new error definition based on the symmetry of the semi-direct product group, and incorporates gravity constraints. The algorithm achieves improved accuracy and robustness without increasing computational resources. Experiments on various public and private datasets show that, compared to existing methods, Eq-LIO can achieve higher accuracy and more importantly, robustness to challenging motion scenes at comparable speeds.

## REFERENCES

- [1] H. Ye, Y. Chen, and M. Liu, "Tightly coupled 3d LiDAR inertial odometry and mapping," in *2019 International Conference on Robotics and Automation (ICRA)*. IEEE, 2019, pp. 3144–3150.
- [2] T. Shan, B. Englot, D. Meyers, W. Wang, C. Ratti, and D. Rus, "LIO-SAM: Tightly-coupled LiDAR inertial odometry via smoothing and mapping," in *2020 IEEE/RSJ international conference on intelligent robots and systems (IROS)*. IEEE, 2020, pp. 5135–5142.
- [3] C. Qin, H. Ye, C. E. Pranata, J. Han, S. Zhang, and M. Liu, "LINS: A LiDAR-inertial state estimator for robust and efficient navigation," in *2020 IEEE international conference on robotics and automation (ICRA)*. IEEE, 2020, pp. 8899–8906.
- [4] F. Aghili and C.-Y. Su, "Robust relative navigation by integration of ICP and adaptive Kalman filter using laser scanner and IMU," *IEEE/ASME Transactions on Mechatronics*, vol. 21, no. 4, pp. 2015–2026, 2016.
- [5] S. Huang and G. Dissanayake, "Convergence and consistency analysis for extended Kalman filter based SLAM," *IEEE Transactions on robotics*, vol. 23, no. 5, pp. 1036–1049, 2007.
- [6] A. Barrau and S. Bonnabel, "The invariant extended Kalman filter as a stable observer," *IEEE Transactions on Automatic Control*, vol. 62, no. 4, pp. 1797–1812, 2016.
- [7] P. Shi, Z. Zhu, S. Sun, X. Zhao, and M. Tan, "Invariant extended Kalman filtering for tightly coupled LiDAR-inertial odometry and mapping," *IEEE/ASME Transactions on Mechatronics*, vol. 28, no. 4, pp. 2213–2224, 2023.
- [8] P. van Goor, T. Hamel, and R. Mahony, "Equivariant filter (EqF)," *IEEE Transactions on Automatic Control*, vol. 68, no. 6, pp. 3501–3512, 2022.
- [9] P. van Goor and R. Mahony, "EqVIO: An equivariant filter for visual-inertial odometry," *IEEE Transactions on Robotics*, vol. 39, no. 5, pp. 3567–3585, 2023.
- [10] J. Zhang, S. Singh *et al.*, "LOAM: LiDAR odometry and mapping in real-time," in *Robotics: Science and systems*, vol. 2, no. 9. Berkeley, CA, 2014, pp. 1–9.
- [11] S. Hening, C. A. Ippolito, K. S. Krishnakumar, V. Stepanyan, and M. Teodorescu, "3D LiDAR SLAM integration with GPS/INS for UAVs in urban GPS-degraded environments," in *AIAA Information Systems-AIAA Infotech@ Aerospace*, 2017, p. 0448.
- [12] K. Chen, B. T. Lopez, A.-a. Agha-mohammadi, and A. Mehta, "Direct LIDAR odometry: Fast localization with dense point clouds," *IEEE Robotics and Automation Letters*, vol. 7, no. 2, pp. 2000–2007, 2022.
- [13] W. Xu and F. Zhang, "FAST-LIO: A fast, robust LiDAR-inertial odometry package by tightly-coupled iterated Kalman filter," *IEEE Robotics and Automation Letters*, vol. 6, no. 2, pp. 3317–3324, 2021.
- [14] W. Xu, Y. Cai, D. He, J. Lin, and F. Zhang, "FAST-LIO2: Fast direct LiDAR-inertial odometry," *IEEE Transactions on Robotics*, vol. 38, no. 4, pp. 2053–2073, 2022.
- [15] R. Hartley, M. Ghaffari, R. M. Eustice, and J. W. Grizzle, "Contact-aided invariant extended Kalman filtering for robot state estimation," *The International Journal of Robotics Research*, vol. 39, no. 4, pp. 402–430, 2020.
- [16] C. Liu, C. Jiang, and H. Wang, "InGVIO: A consistent invariant filter for fast and high-accuracy GNSS-visual-inertial odometry," *IEEE Robotics and Automation Letters*, vol. 8, no. 3, pp. 1850–1857, 2023.
- [17] H. Zhang, R. Xiao, J. Li, C. Yan, and H. Tang, "A high-precision LiDAR-inertial odometry via invariant extended Kalman filtering and efficient surfel mapping," *IEEE Transactions on Instrumentation and Measurement*, 2024.
- [18] R. Mahony, T. Hamel, and J. Trumpf, "Equivariant systems theory and observer design," *arXiv preprint arXiv:2006.08276*, 2020.
- [19] A. Fornasier, Y. Ng, R. Mahony, and S. Weiss, "Equivariant filter design for inertial navigation systems with input measurement biases," in *2022 International Conference on Robotics and Automation (ICRA)*. IEEE, 2022, pp. 4333–4339.
- [20] A. Fornasier, Y. Ge, P. van Goor, R. Mahony, and S. Weiss, "Equivariant symmetries for inertial navigation systems," *arXiv preprint arXiv:2309.03765*, 2023.
- [21] A. Fornasier, P. van Goor, E. Allak, R. Mahony, and S. Weiss, "MSCEqF: A multi state constraint equivariant filter for vision-aided inertial navigation," *IEEE Robotics and Automation Letters*, vol. 9, no. 1, pp. 731–738, 2023.
- [22] A. Fornasier, Y. Ng, C. Brommer, C. Böhm, R. Mahony, and S. Weiss, "Overcoming bias: Equivariant filter design for biased attitude estimation with online calibration," *IEEE Robotics and Automation Letters*, vol. 7, no. 4, pp. 12 118–12 125, 2022.
- [23] P. van Goor and R. Mahony, "An equivariant filter for visual inertial odometry," in *2021 IEEE International Conference on Robotics and Automation (ICRA)*. IEEE, 2021, pp. 14 432–14 438.
- [24] K. Wu, T. Zhang, D. Su, S. Huang, and G. Dissanayake, "An invariant-ekf VINS algorithm for improving consistency," in *2017 IEEE/RSJ international conference on intelligent robots and systems (IROS)*. IEEE, 2017, pp. 1578–1585.
- [25] R. Mahony, P. Van Goor, and T. Hamel, "Observer design for nonlinear systems with equivariance," *Annual Review of Control, Robotics, and Autonomous Systems*, vol. 5, no. 1, pp. 221–252, 2022.
- [26] C. Hertzberg, R. Wagner, U. Frese, and L. Schröder, "Integrating generic sensor fusion algorithms with sound state representations through encapsulation of manifolds," *Information Fusion*, vol. 14, no. 1, pp. 57–77, 2013.
- [27] D. He, W. Xu, and F. Zhang, "Symbolic representation and toolkit development of iterated error-state extended Kalman filters on manifolds," *IEEE Transactions on Industrial Electronics*, vol. 70, no. 12, pp. 12 533–12 544, 2023.
- [28] K. Li, M. Li, and U. D. Hanebeck, "Towards high-performance solid-state-LiDAR-inertial odometry and mapping," *IEEE Robotics and Automation Letters*, vol. 6, no. 3, pp. 5167–5174, 2021.
- [29] J. Lin and F. Zhang, "R3LIVE: A robust, real-time, rgb-colored, LiDAR-inertial-visual tightly-coupled state estimation and mapping package," in *2022 International Conference on Robotics and Automation (ICRA)*, 2022, pp. 10 672–10 678.